

<https://doi.org/10.1038/s42003-025-08990-0>

# Proximity labeling unveils potential roles of the Miro2-CISD1 network in mitochondrial dynamics and neuronal differentiation



Im Kyeung Kang<sup>1</sup>, Sunwoo Lee<sup>1</sup>, Tae Kwon Moon<sup>1</sup>, A. Reum Han<sup>2</sup>, Dae Bong Yu<sup>1</sup>, Minkyoo Jung<sup>3</sup>, Chulhwan Kwak<sup>4</sup>, Jeong Kon Seo<sup>5</sup>, Hyun-Woo Rhee<sup>4</sup>, Seong Who Kim<sup>2,6</sup>, Ha-Na Woo<sup>2,6</sup>✉, Ji Young Mun<sup>3</sup>✉ & Heuiran Lee<sup>1,6</sup>✉

Adult hippocampal neurogenesis, crucial for maintaining neural homeostasis, is integral to neurodegeneration. We previously identified Miro2 as a key regulator of mitochondrial dynamics and survival in hippocampal neural stem cells with potential relevance to Alzheimer's disease. Here, using TurboID-based proximity labeling, we explore Miro2's interaction networks and identify sixty-six unique interactors specific to hippocampal neural stem cells. Functional enrichment analysis reveals that these proteins are crucial for mitochondrial organization, transport, and neurodegeneration. CISD1 emerges as a significant interaction partner. Knockdown of Miro2 and CISD1 impairs mitochondrial trafficking in adult hippocampal stem cells, disrupted stem cell differentiation with increased cytotoxicity. Rescue experiments partially reverse cell death, and both Miro2 and CISD1 show increased expression and interaction during differentiation. These findings suggest the Miro2–CISD1 axis as a critical regulator of mitochondrial remodeling and neurogenesis, providing a framework for future studies on how mitochondrial dynamics contribute to neurodegenerative disease mechanisms.

Hippocampal neural stem (HCN) cells are essential for adult neurogenesis, generating new neurons in the subgranular zone of the hippocampal dentate gyrus and the subventricular zone of the lateral ventricle<sup>1</sup>. Brain injuries stimulate HCN cell proliferation and differentiation, enabling migration and integration into neural networks for functional recovery. Impairments in neurogenesis are linked to neurodegenerative diseases<sup>2,3</sup>. Isolated from the adult rat brain by the Gage group, HCN cells differentiate into neurons, astrocytes, and oligodendrocytes both in vitro and in vivo, influenced by various factors. The HCN cells exhibit a unique susceptibility to autophagy-dependent cell death (ADCD) under conditions of insulin withdrawal<sup>4,5</sup>. Our previous study demonstrated that miR-351-5p targets Miro2, reducing its levels and inducing ADCD. The results indicated that mitochondrial dysfunction, fission, and subsequent mitophagy-dependent cell death occur

during HCN cell death via the miR-351-5p/Miro2 axis. It also provided evidence that Miro2 decreased in Alzheimer's disease models.

Mitochondria are dynamic subcellular organelles essential for various cellular processes, including energy metabolism and cell survival<sup>6,7</sup>. Dysregulated mitochondrial dynamics contribute to neurodegenerative disorders like Alzheimer's and Parkinson's disease<sup>8,9</sup>. Miro proteins (Miro1 and Miro2) are mitochondrial outer membrane GTPases critical for mitochondrial trafficking, dynamics, mitophagy, calcium homeostasis, mitochondria-ER contacts, and mitochondrial transfer through their interactions with the cytoskeleton and other cellular components<sup>10–12</sup>. Miro enables bidirectional mitochondrial transport by interacting with Milton along with motor proteins like kinesin and dynein<sup>13</sup>. While several Miro2 interactors have been identified, our comprehension of the functional

<sup>1</sup>Department of Microbiology, Asan Medical Institute of Convergence Science and Technology, Asan Medical Center, University of Ulsan College of Medicine, Seoul, Republic of Korea. <sup>2</sup>Department of Biochemistry and Molecular Biology, University of Ulsan College of Medicine, Seoul, Republic of Korea. <sup>3</sup>Neural Circuit Research Group, Korea Brain Research Institute, Daegu, Republic of Korea. <sup>4</sup>Department of Chemistry, Seoul National University, Seoul, Republic of Korea.

<sup>5</sup>Department of UNIST Central Research Facilities, Ulsan National Institute of Science and Technology, Ulsan, Republic of Korea. <sup>6</sup>Bio-Medical Institute of Technology, University of Ulsan College of Medicine, Seoul, Korea. ✉e-mail: [woohn101@gmail.com](mailto:woohn101@gmail.com); [jymun@kbri.re.kr](mailto:jymun@kbri.re.kr); [heuiran@amc.seoul.kr](mailto:heuiran@amc.seoul.kr)

network and action mechanisms involving Miro2 on mitochondria remains limited and fragmented. Further in-depth studies are needed to elucidate how these interactors contribute to these critical cellular processes.

Protein interaction networks and compartmentalization are fundamental to cellular signaling. Traditional methods for studying protein–protein interactions, including immunoprecipitation and yeast two-hybrid assays, have limitations such as non-specific contamination by non-specific molecules and subcellular bias. Recently, enzyme-catalyzed proximity labeling has emerged as a powerful alternative for studying the spatial and interaction characteristics of proteins in living cells by biotinylating nearby proteins in living cells for streptavidin enrichment and mass spectrometry identification<sup>13</sup>. TurboID, an engineered biotin ligase, enables rapid, efficient labeling of proximal proteins<sup>14–16</sup>.

To this end, TurboID-based proximity labeling was utilized to map the spatial proteomes and interaction networks within HCN cells, focusing on Miro2’s protein–protein interactions with potential partners. This approach seeks to deepen our understanding of Miro2’s mitochondrial roles and its influence on neurogenesis in HCN cells.

## Results

### Proximity labeling systems were validated and applied to uncover Miro2 interactome

Miro2-TurboID (Miro2-TID) and TurboID-Miro2 (TID-Miro2) fusion protein constructs were generated by cloning Miro2 into the N- or C-terminus of TurboID (Fig. 1a). Following optimization in 293T cells, a

50 μM biotin treatment for 6 h was chosen to maximize labeling efficiency while minimizing non-specific background, ensuring high-fidelity capture of Miro2-interacting proteins (Supplementary Fig. 1). All constructs successfully expressed the fusion proteins as expected and demonstrated effective biotinylation (Fig. 1b). The subcellular distribution of the constructs in HeLa cells was analyzed to determine if the bait proteins maintained their native subcellular localization (Fig. 1c). Similar to Tom20-TID, TID-Miro2 showed mitochondrial localization, whereas Miro2-TID, like TID alone, remained cytosolic. Quantitative colocalization analysis indicated that TID-Miro2 exhibits strong mitochondrial targeting, as reflected by a Pearson’s coefficient of  $0.95 \pm 0.00$  and an overlap coefficient of  $0.96 \pm 0.00$  (Fig. 1d, e). MitoTracker staining and mitochondrial motility assays suggested no detectable alterations in mitochondrial morphology or dynamics across HCN-TurboID cell lines (Supplementary Fig. 2), indicating that TID-Miro2 preserves endogenous Miro2 function and is suitable for proximity labeling. To overcome low transfection efficiency in HCN cells, we generated stable cell lines using a lentiviral system and confirmed successful enrichment of biotinylated proteins prior to mass spectrometry (Supplementary Figs. 3–4). Following biotinylation and trypsin digestion, biotinylated peptides were isolated, and lysine residues modified by biotin (K + 226 Da) were analyzed by liquid chromatography-tandem mass spectrometry (LC-MS/MS) (Fig. 2a; Supplementary Fig. 5). Biotin-modified site analysis or super-resolution proximity labeling workflow can provide a clear picture of proximal biotinylated interactome, as shown in previous studies<sup>17,18</sup>. On average, 950 Miro2-enriched, 918 Tom20-enriched, and

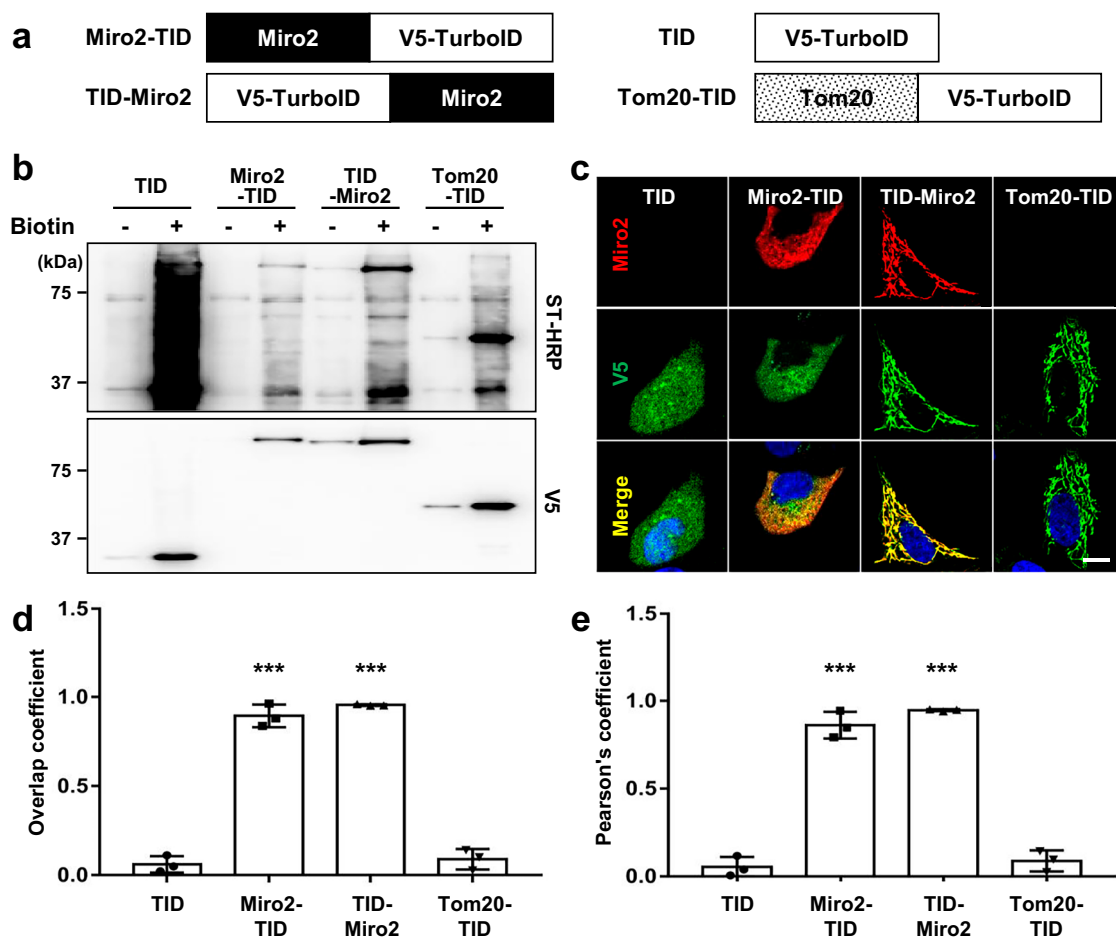


**Fig. 1 | TurboID-based proximity labeling system verification.** **a** Construction of plasmid for proximity labeling. All the plasmids contained a V5 tag. **b** Streptavidin-horseradish peroxidase (SA-HRP) and anti-V5 western blotting under the expression of TurboID constructs (i.e., TID, Miro2-TID, TID-Miro2, and Tom20-TID) in 293T cells. **c** Anti-Miro2 and V5 immunofluorescence results for the expression of

TurboID constructs in HeLa cells. The scale bar represents 10 μm. **d** Pearson’s coefficient of TurboID constructs. Miro2-TID \*\*\**p* = 0.0001, TID-Miro2 \*\*\**p* < 0.0001. **e** Overlap coefficient of TurboID constructs. \*\*\**p* < 0.0001. *n* = 3 biologically independent experiments. The data represent the means ± SDs.

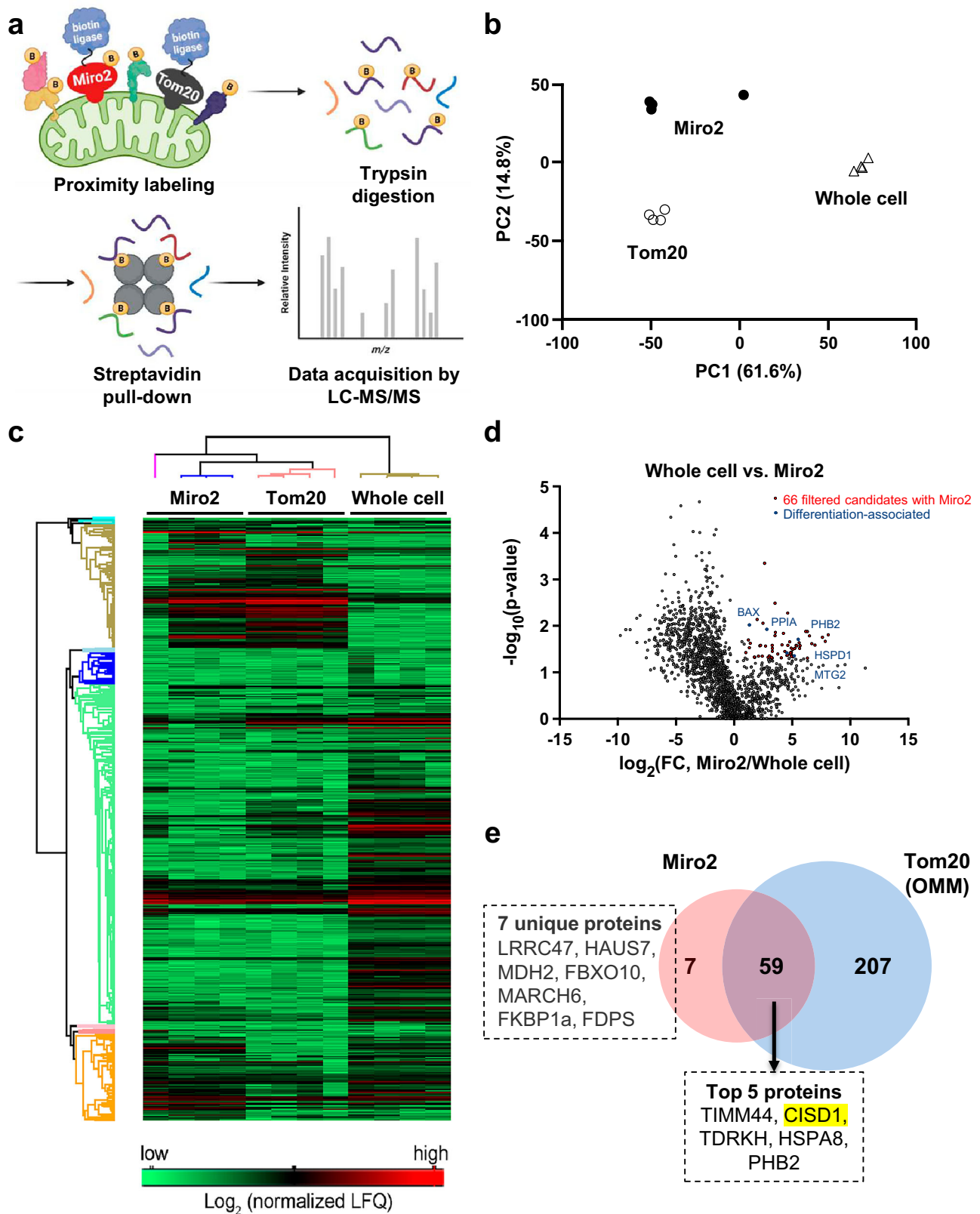


**Fig. 2 | Miro2 proximal protein identification.** **a** Schematic of the process used to obtain the enriched Miro2-interacting proteins. **b** PCA plot showing the segregation of the identified interactomes between the control (Whole cell, Tom20) and the Miro2 interactome (Miro2) across the two PCA axes. Data points for Miro2 (solid circles), Tom20 (white circles), and Whole cell (triangles); four biological replicates are shown. The percentages correspond to the relative contribution of each axis to the overall variation in protein expression. **c** Heatmap of the  $\log_2$ -fold change (FC)

in the abundance of proteins identified for each sample with Miro2, Tom20 and Whole cell enrichment. **d** Volcano plots display quantified protein interactors of Miro2 compared with those in the Whole cell. Red dots represent enriched proteins (fold change  $\geq 2$ ,  $p$ -value  $< 0.05$ ). **e** Venn diagram of Miro2 interactors shows unique and overlapping interactors of Miro2 and Tom20, which are filtered by Whole-cell interactors.

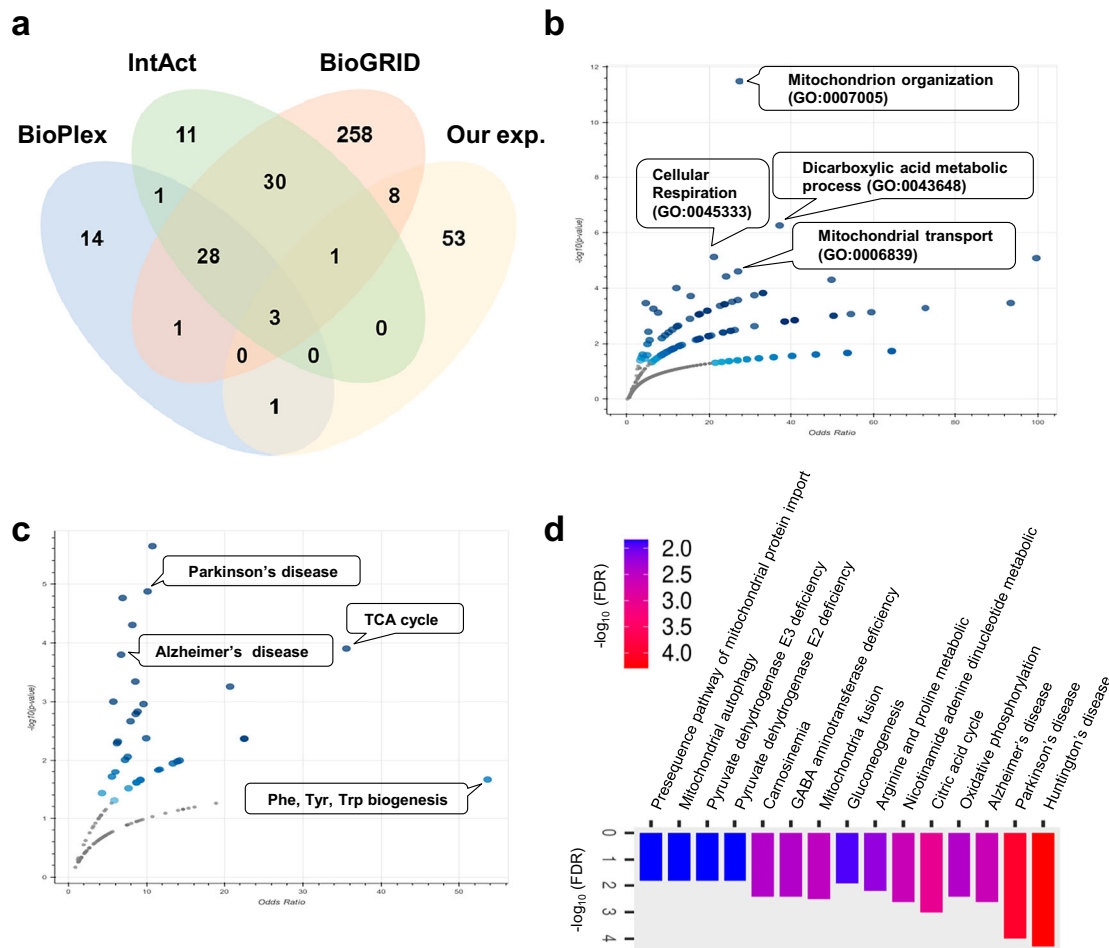


**Fig. 3 | Miro2 proximal protein functional annotations.** **a** Venn diagram of Miro2 interactors shows the overlapping proteins between our experiment and other references. (i.e., Biophysical Interactions of ORFeome-based Complexes (BioPlex), IntAct, and Biological General Repository for Interaction Datasets (BioGRID)) and

the unique proteins in our experiment. **b** Dot plot of the most significant GO biological processes and **c** KEGG pathways associated with Miro2 interactors. **d** Bar plot of ShinyGO 0.80 enrichment analysis data (top 15) associated with Miro2 interactors.

1489 cytosol-enriched interactors were identified. Principal component analysis revealed that 61.6% and 14.8% of the interactome variation, respectively, represented by principal components 1 (PC1) and 2 (PC2), and each cluster further exhibited a distinct separation of protein profiles (Fig. 2b). Hierarchical cluster analysis showed high concordance between replicates of each experimental group and revealed a distinct interaction profile for Miro2-enriched proteins compared to Tom20 (Ctrl2) and Whole cell (Ctrl1), with unique patterns among the groups (Fig. 2c).

### Miro2 interactome was assessed using interactome databases

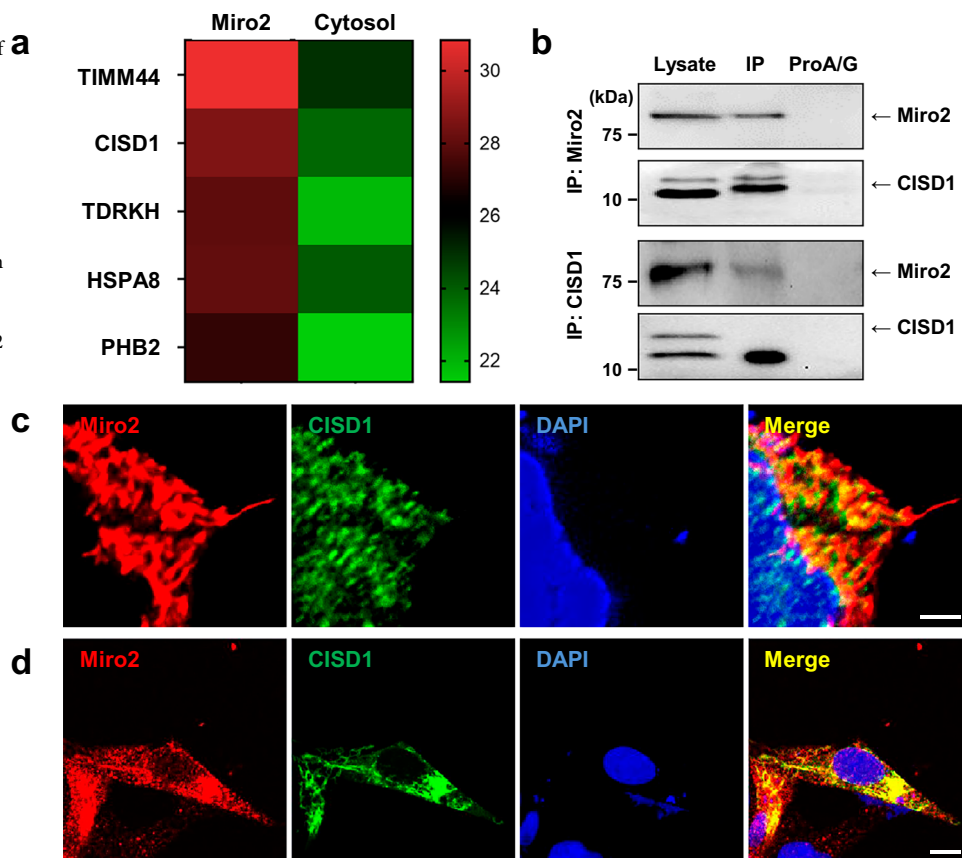
The major changes that met the criteria for quantitative MS analysis between Miro2 and Whole cell and between Tom20 and Whole cell were displayed in volcano plots (Fig. 2d, Supplementary Fig. 6). Sixty-six proteins were identified as Miro2 interactors with significantly altered abundance compared to the Whole cell, whereas Tom20 interactors numbered 266 under similar conditions. Among these proteins, seven proteins were Miro2 specific and 59 overlapped with Miro2 and Tom20 (Fig. 2e, and Supplementary Table 1). The specificity of our findings, using Miro2 as a keyword to explore network-based resources for protein–protein interaction studies, was assessed by comparing them with existing interactome databases, such as BioPlex (Biophysical Interactions of ORFeome-based Complexes), IntAct, and BioGRID (Biological General Repository for Interaction Datasets) (Fig. 3a). The results indicated that among the proteins identified as Miro2 interactors, only thirteen were found in previously reported interactome databases. These findings highlight the distinctive Miro2

interactome specific to neural stem cells (NSCs) and reveal previously undocumented interactors not found in existing databases. In addition, we performed Gene Ontology analyses of the Miro2-interacting protein hits to evaluate their reported biological processes. The top biological processes included mitochondrion organization (GO:0007005), mitochondrial transport (GO:0006839), and cellular respiration (GO:0045333) (Fig. 3b). The result substantiated the known functions of Miro2 in mitochondria. Interestingly, Kyoto Encyclopedia of Genes and Genomes (KEGG) enrichment analysis demonstrated that Miro2 interactors are strongly associated with neurodegenerative diseases such as Alzheimer's disease and Parkinson's disease (Fig. 3c). ShinyGO 0.80 analysis against various databases and functional categories implied the significant changes in the interactions of these genes with neurodegenerative diseases, as well as in the mitochondrial metabolism and dynamics (Fig. 3d). Overall, these results suggest that Miro2 interactors engage in mitochondrial trafficking and could play a role in neurodegenerative disease pathways.

### The interaction between Miro2 and the candidate interactor C1SD1 was validated

The top five significant hits clustering was represented in Figs. 2e and 4a. The Miro2-specific proximity to these proteins was confirmed by biotinylation experiments in the TurboID cell line (Supplementary Fig. 7). To further explore the functional connectivity of Miro2 with its potential interactors, we examined their known properties, including subcellular localization, activity, and biological functions, focusing on those particularly

**Fig. 4 | Verification of the interaction between Miro2 and CISD1 in the cells. a** Top 5 heatmaps of  $\log_2$  (FC) abundances for Miro2 interactors. **b** Coimmunoprecipitation of endogenous Miro2 and CISD1 in HCN cells. **c** Immunofluorescence images of colocalization of Miro2 and CISD1 in HCN cells overexpressing Myc-Miro2. Miro2 was stained with anti-Myc antibody and CISD1 was stained with anti-CISD1 antibody. Yellow areas within merging images indicate that co-localization of Miro2 and CISD1. Nucleus was stained with DAPI. Scale bar: 2  $\mu$ m. **d** Immunofluorescence images of SH-SY5Y cells overexpressing Myc-Miro2 and HA-CISD1. Miro2 was stained with anti-Myc antibody and CISD1 was stained with anti-HA antibody. Scale bar: 10  $\mu$ m.



relevant to NSCs. Among the top five Miro2 interactors, CISD1 (CDGSH Iron Sulfur Domain 1) was the only protein localized to the mitochondrial outer membrane, similar to Miro2, and has been identified as an early-stage biomarker of Alzheimer's disease linked to mitochondrial dysfunction<sup>19</sup>. STRING analysis revealed that CISD1 clusters with proteins involved in mitochondrial regulation and stem cell differentiation, including TIMM44, PHB2, and HSPA8, highlighting its potential functional relevance (Supplementary Fig. 8). In light of these findings, CISD1 was selected for further investigation as a potential Miro2 interactor. Reciprocal immunoprecipitation of endogenous proteins in HCN cells confirmed an interaction between Miro2 and CISD1 (Fig. 4b). The dominance of yellow color in the immunocytochemistry experiment indicates colocalization of Miro2 and CISD1 proteins within the same region in HCN cells (Fig. 4c). The coefficient values prove this; Pearson's coefficient 0.66 ( $\pm$  0.13) and Overlap coefficient 0.77 ( $\pm$  0.11). Colocalization of Miro2 and CISD1 was further confirmed by overexpression of Myc-Miro2 and HA-CISD1 tagged constructs in neuroblastoma SH-SY5Y cells (Fig. 4d). The coefficient values prove this; Pearson's coefficient 0.85 ( $\pm$  0.06) and Overlap coefficient 0.89 ( $\pm$  0.05). Taken together, these data indicate a correlated interaction between Miro2 and CISD1 and support the reliability of the Miro2 interactome data.

#### Miro2 and CISD1 regulate mitochondrial trafficking

To investigate the cellular function of Miro2 and CISD1 in HCN cells, we specifically knocked down these proteins (Supplementary Fig. 9) and then observed the mitochondria using transmission electron microscopy. When Miro2 and CISD1 were suppressed, mitochondria in HCN cells became shortened and fragmented (Fig. 5a). We confirmed the mitochondrial morphological changes by measuring the aspect ratio (Fig. 5c). Additionally, the distribution of mitochondria in Miro2 and CISD1 knockdown cells was quite distinct from that observed in siCON-treated cells (Fig. 5b). In Miro2

and CISD1 knockdown cells, mitochondria were positioned closer to the nucleus, suggesting reduced mitochondrial movement. The Imaris program was used to measure the distance between the mitochondria and the nucleus, revealing that the knockdown of Miro2 and CISD1 resulted in a reduced distance between the nucleus and mitochondria (Fig. 5d). These results thus imply that CISD1, like Miro2, is a major factor influencing mitochondrial trafficking.

#### Miro2 and CISD1 enable the differentiation of hippocampal neural stem cells

One of the key characteristics of NSCs is their ability to differentiate into cells of the nervous system<sup>20,21</sup>. To investigate the roles of Miro2 and CISD1 in neuronal differentiation, we analyzed protein expression changes during this process, confirming HCN cells' differentiation potential through immunocytochemistry of several markers. Results indicated that undifferentiated HCN cells strongly expressed Nestin and PAX6, specific to NSCs, while differentiated cells exhibited MAP2 along neurites and a low detection rate of the astrocyte marker GFAP (Fig. 6a). Furthermore, under these differentiation conditions, the levels of both Miro2 and CISD1 proteins significantly increased (Fig. 6b, c). Inducing neural differentiation under Miro2 and CISD1 knockdown led to a significant increase in cell death (Fig. 6d). The LDH assay consistently showed elevated cytotoxicity in Miro2 and CISD1 downregulated groups, compared to siCON (Fig. 6e). Rescue experiments demonstrated that overexpression of either Miro2 or CISD1 reduced knockdown-induced cell death and partially restored neuronal differentiation (Supplementary Fig. 10). Under differentiation conditions, protein levels of both Miro2 and CISD1 increased, and co-immunoprecipitation assays revealed a concomitant enhancement in their interaction (Supplementary Fig. 11). This interaction increase was specific to the Miro2–CISD1 pair, as no change was detected for Drp1 or TIMM44, despite their presence in the Miro2 interactome. These results

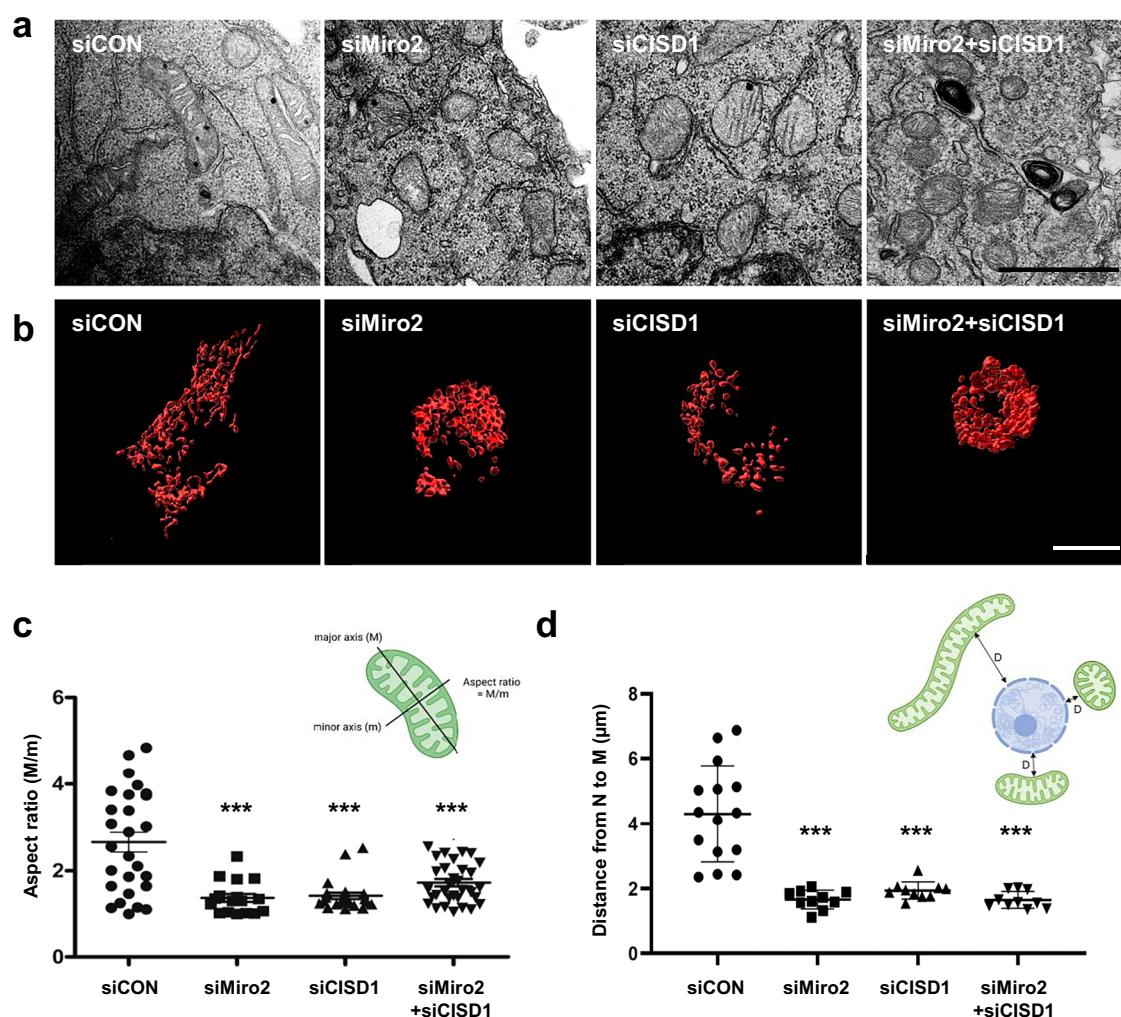


**Fig. 5 | Investigation of Miro2 and CISD1 involvement on mitochondria.**

**a** Representative transmission electron microscopy images acquired after transfection of siMiro2 and/or siCISD1. Scale bar: 1  $\mu$ m. **b** Reconstructed images of TMRM-stained mitochondria following Miro2 and/or CISD1 knockdown, processed using the Imaris program. Scale bar: 10  $\mu$ m. **c** Quantification of aspect ratio (M/m) after Miro2 and CISD1 siRNA treatment. “M” and “m” represent the major and minor

axes of mitochondria, respectively. Created in BioRender. Woo, H. (2025) <https://BioRender.com/ije8ur1>. **d** Quantification of the distance from the nucleus to the mitochondria after Miro2 and CISD1 siRNA treatment. “D” represents the distance from the nucleus to the mitochondria. Created in BioRender. Woo, H. (2025) <https://BioRender.com/nygjckv>.  $n = 3$ , 15 mitochondria per cell, biologically independent experiments. \*\*\* $p = 0.0000$ . The data in the graphs represent the means  $\pm$  SDs.

indicate that Miro2 and CISD1 expression and physical association are both upregulated during neuronal differentiation and that their knockdown impairs cell survival and differentiation capacity.

### Discussion

In this study, we successfully mapped the Miro2 interactome in HCN cells using proximity labeling, expanding on our prior findings that Miro2 is crucial in Alzheimer’s disease and related dementias by regulating mitochondrial dynamics. Our integrative analysis, which incorporated bioinformatics tools and public database resources, revealed that Miro2 interactors primarily linked with mitochondrial maintenance and beta-oxidation of fatty acids. Interestingly, the KEGG and ShinyGO analyses revealed a significant correlation between the Miro2 interactome and neurodegenerative disease, suggesting that these findings may reflect the distinctive characteristics of HCN cells. Previous studies have shown that a sharp decline of adult hippocampal neurogenesis has been observed in early Alzheimer’s disease<sup>2,3</sup>. Enhancing the viability of HCN cells may help mitigating neurodegenerative diseases associated with a reduced NSC pool<sup>22,23</sup>. Additionally, the upregulation of Miro2 and its key interactor CISD1 during neural differentiation suggests that these proteins support cell viability, probably facilitating differentiation. While many of the identified

interactors are enriched in mitochondrial pathways, some—such as HSPD1, PPIA, and PHB2—have also been implicated in stem cell differentiation. This suggests that mitochondrial proteins may play dual roles in both supporting cellular metabolism and regulating neurogenesis. This study enhances our understanding of the role of Miro2 by detailing its interactome in HCN cells and emphasizing its critical influence on mitochondrial trafficking and neurogenesis.

TurboID offers high efficiency and minimal toxicity in proximity labeling, allowing accurate interaction detection within living cells based on protein subcellular localization. Although advantageous, proximity labeling has limitations, including the need to express the biotin ligase as a fusion protein with the bait and the requirement for high overexpression in cell lines like 293T. To address this, we created two Miro2-TurboID fusion variants and verified their correct subcellular localization. To improve low transfection efficiency in HCN cells, we established stable cell lines using a lentivirus system<sup>24,25</sup>. Given their ability to effectively transduce both dividing and non-dividing cells, lentiviral vectors serve as adequate transgene delivery tools, as they also result in stable and long-term gene expression.

The reliability of our results is supported by the overlap with proteins listed in interactome databases and the validation of recognized proteins, such as TRAK1 and MYO19, as demonstrated in previous studies<sup>26,27</sup>. The

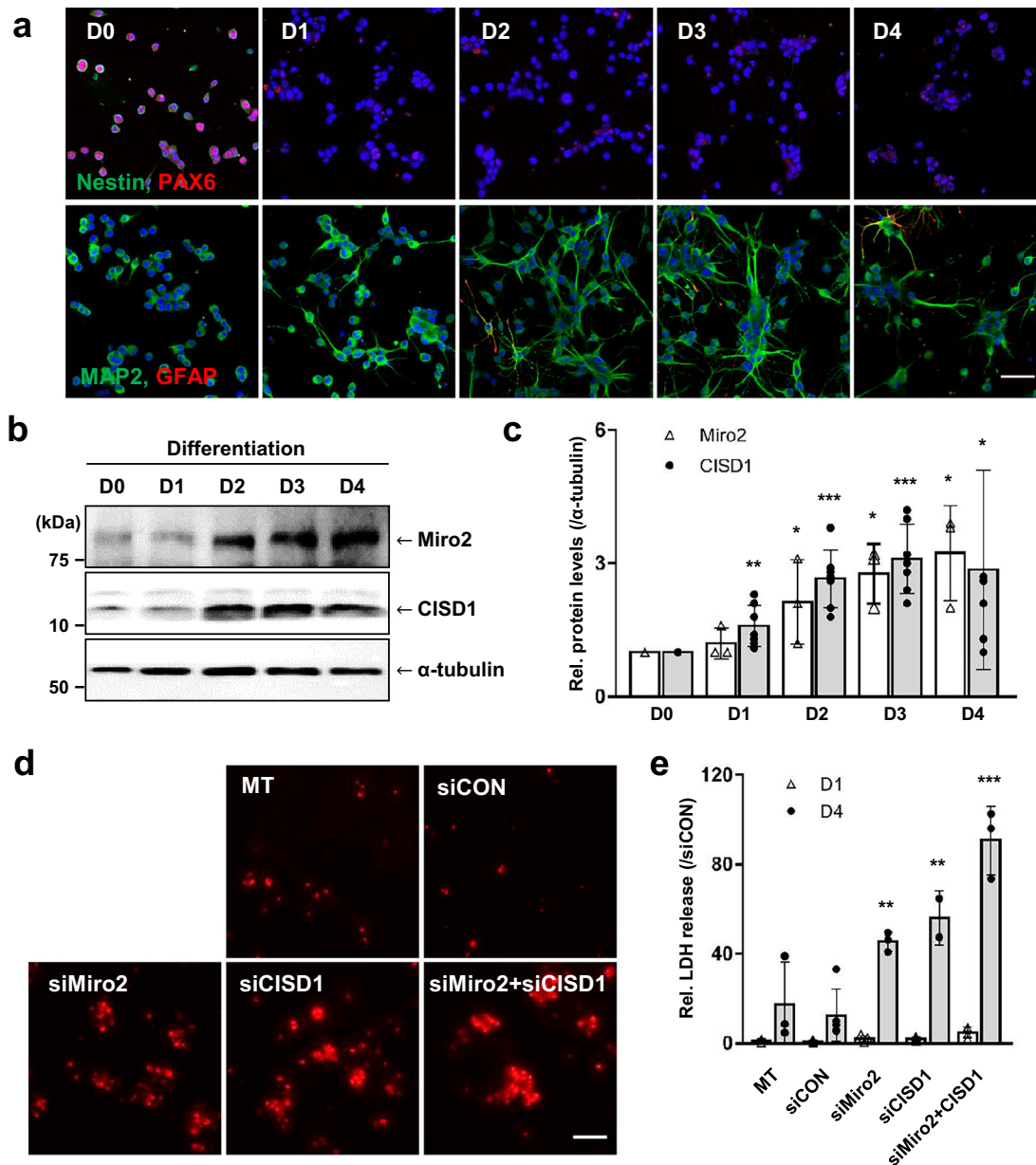


**Fig. 6 | Suppression of HCN cell differentiation under the downregulation of Miro2 and CISD1.** **a** Examination of capacity of neural differentiation of the cells. After induction of differentiation using retinoic acid and forskolin, the cells were stained with Nestin and PAX6 which are NSC-specific markers, at the indicated time point. Nestin (green) and PAX6 (red) show high intensity signals in undifferentiated HCN cells (D0) and decrease signal with differentiation. The cells were stained with MAP2, a neuronal marker and GFAP, an astrocyte marker. MAP2 (green) was stained along the neurites. GFAP (red) was rarely stained. **b** Western blot analysis of Miro2 and CISD1 during 4 days after differentiation (D0–D4). **c** Quantification of the amount of Miro2 and CISD1 proteins during 4 days of differentiation.  $n = 3–7$  biologically independent experiments. Miro2: D1  $p = 0.5646$ , D2  $*p = 0.0561$ , D3

$*p = 0.0226$ , D4  $*p = 0.0317$ , CISD1: D1  $**p = 0.0053$ , D2  $***p = 0.0000$ , D3  $***p = 0.0000$ , D4  $*p = 0.0488$ . **d** HCN cells were stained with PI at D4 of differentiation following siRNA treatment. Suppression of Miro2 and CISD1 induced cell death in the cells. Scale bar: 50  $\mu\text{m}$ . **e** Lactate dehydrogenase (LDH) release assay on D1 and D4 of differentiation following Miro2 and CISD1 siRNA treatment in HCN cells. Relative LDH release increased at D4 in the siRNA treated group compared with MT (no treated) and siCON group. Both siMiro2 and siCISD1 treated groups significantly increased in LDH.  $n = 3–7$  biologically independent experiments. D4; siMiro2  $**p = 0.0037$ , siCISD1  $**p = 0.0068$ , siMiro2+siCISD1  $***p = 0.0002$ . The data in the graphs represent the means  $\pm$  SDs.

interactions of other proteins with Miro have also been documented. Specifically, the mitochondrial fusion proteins mitofusin 1 (MFN1) and mitofusin 2 (MFN2) affect mitochondrial dynamics through interaction with Miro. MFN2 is directly involved in mitochondrial transport in axons by interacting with the Miro/Milton complex<sup>28</sup>. Miro also acts as a sensor for cytosolic  $\text{Ca}^{2+}$  ( $\text{cCa}^{2+}$ ), with the EF-hand domain. An increase in  $\text{cCa}^{2+}$  triggers the dissociation of the N-terminus of the mitochondrial calcium uniporter (MCU), disrupting the MCU-Miro interaction, which is crucial for maintaining mitochondrial transport in axon cells<sup>29</sup>. Notably, the Miro

protein exists in two isoforms, designated Miro1 and Miro2<sup>30,31</sup>. The two isoforms share key features, including the GTPase domain and EF hands. They are also known to form heterodimers, but prior studies have often not differentiated between the two isoforms or have mostly focused on Miro1<sup>32</sup>. However, our previous study suggests that there may be functional differences between the two proteins<sup>5</sup>. Additionally, an analysis of interactome databases revealed that Miro1 and Miro2 exhibit distinct patterns of protein interaction. Further investigations of these differences based on interactome analysis would be promising.

Utilizing Miro2 as a keyword, we can leverage publicly accessible databases to further investigate and understand the functional roles of Miro2. However, several limitations must be acknowledged. The Bioplex dataset is restricted to Miro2 interactome data from 293 and HCT116 cell lines, while IntAct predominantly focuses on human data. Although BioGRID provides extensive data from various analytical methods, it still lacks species diversity, underscoring the need for additional data to enhance reliability. Notably, we found limited interactome data derived specifically from NSCs. Considering the unique characteristics of these cells, we anticipate that our Miro2 interactome will provide meaningful insights into the functional role of Miro2 in neuronal systems. As expected, the Miro2 interactors identified in our study show minimal overlap with those identified in public databases. Nonetheless, 80.3% of proteins uniquely found in our study represent key entities that could advance our understanding of the specific role of Miro2 in HCN cells and its potential links to neurodegenerative diseases.

This study identified CISD1 as a Miro2 interactor with a high *p*-value, uncovering previously unknown functions of CISD1 associated with its interaction with Miro2. CISD1 is known to form a homodimer and resided to the contact site between the mitochondrial outer membrane and the ER membrane<sup>33–35</sup>. Recent findings suggested that it is crucial for intracellular calcium homeostasis and inhibits ferroptosis by preventing mitochondrial lipid peroxidation<sup>36,37</sup>. Moreover, CISD1 has recently been identified as a previously unrecognized early-stage biomarker of Alzheimer's disease, unlike the established markers VGF, LTF, PARP1, and MAOA. CISD1 deficiency in mice has been linked to cognitive impairment and increased neuroinflammation<sup>19,38,39</sup>. Our study further demonstrates that CISD1, together with Miro2, plays a critical role in regulating mitochondrial trafficking. Interestingly, CISD1 knockdown in undifferentiated HCN cells did not markedly affect cell viability but increased the co-localization of Mitotracker and LysoTracker signals (Supplementary Fig. 12), indicating a previously unreported link between CISD1 and Miro2-mediated mitochondrial trafficking in maintaining mitochondrial integrity. We also found that Miro2 and CISD1 contribute to neural differentiation through increased expression, enhanced interaction, and support of cell survival. During the differentiation of NSCs into neurons, mitochondrial dynamics are essential, with morphological remodeling reflecting the metabolic state required for this process<sup>40,41</sup>. These findings suggest that Miro2 and CISD1 may act cooperatively to preserve mitochondrial integrity and thereby influence NSC fate, although further epistasis analysis is needed to clarify their mechanistic relationship and confirm their cooperative role in neurogenesis.

In conclusion, utilizing proximity labeling technology, we successfully mapped the functional complexes associated with Miro2 and conducted integrative bioinformatic analyses to provide detailed functional annotations of the Miro2 interactome. These results reveal a distinctive molecular signature within the Miro2 interactome connected to degenerative disorders originating in NSCs. Moreover, CISD1 was identified as a novel regulator of mitochondrial trafficking, shedding light on mechanisms of mitochondrial transport. These findings thus advance our understanding surrounding Miro2.

## Methods

### Adult HCN cell culture, transfection, and differentiation

HCN cells were kindly provided by the laboratory of Dr. Fred Gage. HCN cells were cultured in serum-free Dulbecco's modified Eagle's medium mixture F-12 (Invitrogen) supplemented with 1.27 g/L sodium bicarbonate (Invitrogen), 100 mg/L transferrin (Sigma), 30 nM sodium selenite (Sigma), 16 mg/L putrescine dihydrochloride (Sigma), 20 nM progesterone, 100 µg/mL streptomycin, and 100 U/mL penicillin (Invitrogen). Furthermore, 20 ng/mL fibroblast growth factor β (FGF-β) (Invitrogen) and 5 µg/mL insulin (Sigma) were added to the media before use. All plates for HCN cells were coated with 10 mg/L poly-L-ornithine (Sigma) and 1 mg/L laminin (BD Biosciences). siRNA duplexes were purchased from Bioneer. Transient transfection was conducted using Oligofectamine (Invitrogen) according to the manufacturer's instructions. For differentiation, HCN cells were plated

into coated µ-Dish 35 mm confocal dishes (Ibidi), and 24 h later, the culture medium was replaced with medium containing 1 µM retinoic acid (Tokyo Chemical Industry, # R0064), 5 µM forskolin (Sigma, # F3917), and 0.1% fetal bovine serum (Corning #35-015-CV)<sup>42</sup>.

### Cell viability assays

To identify the cytotoxicity during differentiation, LDH in conditioned medium was measured using the LDH release assay (Promega, # J2380). Viability was measured by staining with Hoechst 33342 and PI. Hoechst 33342 (5 µg/mL) and PI (1 µg/mL) were added to the culture media, and cells were maintained at 37 °C. After 5 min, the observed fields were randomly selected (> 8 fields, > 200 cells/field) and imaged under a fluorescence microscope.

### Construction of plasmids

The Tom20-TID plasmid was previously described<sup>43</sup>. The control plasmid, TID, was generated by the elimination of Tom20. To create the Miro2-TID plasmid, the full-length sequences of Miro2 were incorporated into the XhoI site of the TID plasmid. The TID-Miro2 plasmid was constructed by inserting the full-length Miro2 sequence into the KpnI site of the TID plasmid. For lentivirus production, the TID, TID-Miro2, and Tom20-TID cDNA clones were transferred into the pLenti-suCMV vector (GenTarget) via the ClaI/NheI site. All the plasmids contained a V5 tag.

### Proximity labeling and enrichment of biotinylated peptides

Biotin (50 µM) was added to TID, Miro2-TID and Tom20-TID stable cells (100 mm dish, three replicates) for 6 h. After incubation with chilled acetone (4 vol.) with cell lysates at −20 °C for at least 2 h, samples were centrifuged at 13,000 ×g for 10 min at 4 °C. The pellet was resuspended in 500 µL of 8 M urea in 50 mM ammonium bicarbonate. And then, samples were denatured at 650 rpm for 1 h at 37 °C. Sample reduction and alkylation were performed by 10 mM dithiothreitol and 40 mM iodoacetamide at 650 rpm for 1 h at 37 °C. The samples were diluted 8-fold with 50 mM ABC, after which CaCl<sub>2</sub> was added at a final concentration of 1 mM. The samples were digested with trypsin (50:1 w/w) and the insoluble material was removed by centrifugation. After incubating streptavidin beads (150 µL), the samples were washed with 2 M urea in 50 mM ABC two times and washed with pure water. For the elution of the biotinylated peptides from the streptavidin beads, 150 µL of elution solution (80% acetonitrile, 20% water, 0.2% trifluoroacetic acid, and 0.1% formic acid) was incubated with a 60 °C thermomixer three times. The total elution fractions were dried using a HyperVAC SpeedVac (GYROZEN, #VC2200). The samples were stored at −20 °C before use in MS analyses after being cleaned with C18 tips (Thermo Scientific).

### Liquid chromatographic tandem mass spectrometric analysis (LC-MS/MS) and data analysis

The tryptic peptides were analyzed by LC-MS/MS. Analyses were performed on a Q Exactive Plus Orbitrap mass spectrometer (Thermo Fisher Scientific) equipped with a nanoelectrospray ion source. To separate the peptide mixture, we used a C18 reverse-phase HPLC column (500 mm × 75 µm ID) with an acetonitrile/0.1% formic acid gradient from 4 to 32.5% for 120 min at a flow rate of 300 nL/min. For MS/MS analysis, the precursor ion scan MS spectra (*m/z* 400–2000) were acquired in the Orbitrap at a resolution of 70,000 at *m/z* 400 with an internal lock mass. The 15 most intensive ions were isolated and fragmented by high-energy collision-induced dissociation. MS/MS data were analyzed using the MaxQuant platform (version 2.4.2.0) with the Andromeda search engine at a 10 ppm precursor ion mass tolerance against the SwissProt and TrEMBL *Rattus norvegicus* (Rat) proteome databases (92,930 entries, UniProt). The label-free quantification and match-between runs were used with the following search parameters: semi-tryptic digestion, fixed modification with iodoacetamide on cysteine, dynamic oxidation of methionine, protein-N-terminal acetylation, acetylation on lysine, biotinylation on lysine and deamidation on asparagine and glutamine as variable modifications. A false discovery rate of less than 1% was obtained for unique peptides as well as

unique proteins. LFQ intensity values were log<sub>2</sub>-transformed for further analysis, including data normalization, and missing values were filled with imputed values representing a normal distribution around the detection limit. All further processing was conducted under the Perseus package (<https://maxquant.net/perseus/>).

### Bioinformatic analysis of the Miro2 interactome

We used reference databases from BioPlex (<https://bioplex.hms.harvard.edu/explorer/>), IntAct (<https://www.ebi.ac.uk/>), and BioGRID (<https://thebiogrid.org/>). Gene Ontology analysis and pathway enrichment analysis were conducted using Enrichr online server (<https://maayanlab.cloud/Enrichr/>). For pathway enrichment analysis, the Kyoto Encyclopedia of Genes and Genomes (KEGG) 2021 database was utilized to retrieve pathways. A list of differentially expressed proteins generated from the Miro2 interactome was uploaded to the Enrichr tool. Venn diagrams comparing the overlapping proteins identified across the four conditions were generated using the Venn diagram webtool (<https://bioinformatics.psb.ugent.be/webtools/Venn/>).

### Immunoprecipitation and western blot analysis

HCN cells were harvested and lysed in M-per buffer (Thermo Fisher Scientific, 78501) containing protease inhibitors (Merck, P8340) and phosphatase inhibitors (Merck, P5726). The protein contents of the cell lysates were measured using the Pierce bicinchoninic acid protein assay kit (#23225), and 15–20 µg of protein was used for western blot analysis. The primary antibodies used were as follows: anti-Miro2 (1:1000, Proteintech, 11237-1-AP), anti-CISD1 (1:000, Proteintech, 16001-1-AP) and anti-β-actin (1:100,000, Sigma, A5441). After incubating peroxidase-conjugated secondary antibodies with the membrane, images were detected using an enhanced chemiluminescence (ECL) system (Thermo Fisher Scientific, 32106). For immunoprecipitation, HCN cells were lysed in RIPA buffer (10% Triton X-100, 5 M sodium chloride, 1 M HEPES, 0.5 M EDTA, 0.5 M EGTA) containing protease inhibitors and phosphatase inhibitors. 500 µg of cell lysate was incubated overnight with 3 µg of primary antibody, followed by incubation for 1 h with 60 µl of protein A/G magnetic beads (Thermo Fisher Scientific, 88803). The samples were diluted with 1× Laemmli protein sample buffer (Bio-Rad) containing 10% β-mercaptoethanol and heated to denature the proteins. Proteins were loaded with 10–20 µl of lysates. All experiments were conducted in at least three independent biological replicates.

### Immunofluorescence microscopy

HCN cells were prepared in µ-Dish (Ibidi, 81156) and transfected with Miro2 and CISD1 siRNAs for 24 h. After being dyed with MitoTracker™ Deep Red (Invitrogen, M22426), images were obtained using a confocal microscope (Carl Zeiss, LSM 880). The distance between the surface of the nucleus and that of the mitochondria was measured using Imaris (Microscopy Image Analysis Software). HCN cells were stained with markers to confirm their differentiation. Primary antibodies are followed: Nestin (Millipore, # MAB353), PAX6 (Thermo Fisher Scientific, # 5080-RBM3-P0), MAP2 (Millipore, # MAB3418), GFAP (DAKO, # Z0334). Nucleus were stained with DAPI (1 µg/ml).

### Transmission electron microscopy

The cells were prefixed with 2% paraformaldehyde and 2.5% glutaraldehyde in 0.15 M sodium cacodylate buffer (pH 7.4) for 1 h. After washing three times with 0.15 M cacodylate buffer, cells were postfixed in 2% osmium tetroxide (EMS, 19150) with 1.5% ferrocyanide in 0.1 M sodium cacodylate buffer on ice for 1 h. After washing three times in ice-cold ddH<sub>2</sub>O, cells were stained with 1% uranyl acetate (overnight, 4 °C in the dark). For embedding, samples were dehydrated through a graded ethanol series (30, 50, 70, 80, 90, 100, and 100% for 20 min each, 4 °C) followed by epoxy resin infiltration by immersion into 3:1, 1:1, and 1:3 mixtures of ethanol and Epon 812 resin (EMS). Then, samples were incubated in pure resin overnight and placed in an inverted capsule on a confocal dish (70 °C) for 48 h. After trimming, ultrathin serial sections 70 nm thick were cut using an ultramicrotome

(Leica, EM UC7) and mounted on 0.25% formvar coated on hole grids. To enhance the electron density, the sections were stained with UranylLess (EMS, #22409) and 3% lead citrate (EMS, #22410). TEM images were acquired using a Tecnai G220 (Thermo Fisher Scientific) at 120 kV with a US1000XP CCD detector (Gatan).

### Statistics and reproducibility

All the experiments were performed independently (culture batches/transfections) in triplicate or quadruplicate (MS analysis of proximity labeled samples), and all the quantitative results are presented as the means ± standard deviations (SDs). The type of experiments, exact *n* values and *p* values were described in the figure legends. Statistical analysis was performed with Prism 10 software (GraphPad). Student's *t* tests (two-sided) were used to determine statistical significance between the siCON-treated group and an individual siRNA-treated group (siMiro2, siCISD1, siMiro2+siCISD1). Differences between means were considered statistically significant at the following values: \**p* < 0.05, \*\**p* < 0.01, \*\*\**p* < 0.001.

### Reporting summary

Further information on research design is available in the Nature Portfolio Reporting Summary linked to this article.

### Data availability

The datasets supporting the conclusions of this article are available in the ProteomeXchange consortium via MassIVE (<https://massive.ucsd.edu/ProteoSAFe/static/massive.jsp>) repository (Accession no. PXD055479) (Download link) (reviewer ID: reviewer\_pxd055479@ebi.ac.uk, PW: BEA01x5QI5dk). Uncropped blot images are provided in Supplementary Fig. 13. Newly generated plasmids are deposited in Addgene and are available under the following IDs: pLenti-suCMV-TurboID (ID: 247066), pLenti-suCMV-TOM20-TurboID (ID: 247067), pLenti-suCMV-TurboID-Miro2 (ID: 247068). Source data underlying all graphs can be found in Supplementary Data 1. Quantile-normalized entire dataset can be found in Supplementary Data 2.

Received: 1 November 2024; Accepted: 2 October 2025;

Published online: 09 February 2026

### References

- Boldrini, M. et al. Human hippocampal neurogenesis persists throughout aging. *Cell Stem Cell* **22**, 589–599.e585 (2018).
- Salta, E. et al. Adult hippocampal neurogenesis in Alzheimer's disease: a roadmap to clinical relevance. *Cell Stem Cell* **30**, 120–136 (2023).
- Moreno-Jimenez, E. P. et al. Adult hippocampal neurogenesis is abundant in neurologically healthy subjects and drops sharply in patients with Alzheimer's disease. *Nat. Med.* **25**, 554–560 (2019).
- Yu, S. W. et al. Autophagic death of adult hippocampal neural stem cells following insulin withdrawal. *Stem Cells* **26**, 2602–2610 (2008).
- Woo, H. N. et al. miR-351-5p/Miro2 axis contributes to hippocampal neural progenitor cell death via unbalanced mitochondrial fission. *Mol. Ther. Nucleic Acids* **23**, 643–656 (2021).
- Vakifahmetoglu-Norberg, H., Ouchida, A. T. & Norberg, E. The role of mitochondria in metabolism and cell death. *Biochem. Biophys. Res. Commun.* **482**, 426–431 (2017).
- Picard, M. & Shirihai, O. S. Mitochondrial signal transduction. *Cell Metab.* **34**, 1620–1653 (2022).
- Chen, W., Zhao, H. & Li, Y. Mitochondrial dynamics in health and disease: mechanisms and potential targets. *Signal Transduct. Target Ther.* **8**, 333 (2023).
- Su, B. et al. Abnormal mitochondrial dynamics and neurodegenerative diseases. *Biochim. Biophys. Acta* **1802**, 135–142 (2010).
- Li, Y., Yang, Z., Zhang, S. & Li, J. Miro-mediated mitochondrial transport: A new dimension for disease-related abnormal cell metabolism?. *Biochem. Biophys. Res. Commun.* **705**, 149737 (2024).

11. Lacombe, A. & Scorrano, L. The interplay between mitochondrial dynamics and autophagy: from a key homeostatic mechanism to a driver of pathology. *Semin. Cell Dev. Biol.* **161–162**, 1–19 (2024).
12. Marabitti, V., Vulpis, E., Nazio, F. & Campello, S. Mitochondrial transfer as a strategy for enhancing cancer cell fitness: current insights and future directions. *Pharm. Res.* **208**, 107382 (2024).
13. Kay, L., Pienaar, I. S., Cooray, R., Black, G. & Soundararajan, M. Understanding Miro GTPases: implications in the treatment of neurodegenerative disorders. *Mol. Neurobiol.* **55**, 7352–7365 (2018).
14. Cho, K. F. et al. Proximity labeling in mammalian cells with TurboID and split-TurboID. *Nat. Protoc.* **15**, 3971–3999 (2020).
15. Lee, Y. B. & Rhee, H. W. Spray-type modifications: an emerging paradigm in post-translational modifications. *Trends Biochem. Sci.* **49**, 208–223 (2024).
16. Branon, T. C. et al. Efficient proximity labeling in living cells and organisms with TurboID. *Nat. Biotechnol.* **36**, 880–887 (2018).
17. Park, I. et al. Mitochondrial matrix RTN4IP1/OPA10 is an oxidoreductase for coenzyme Q synthesis. *Nat. Chem. Biol.* **20**, 221–233 (2024).
18. Shin, S. et al. Super-resolution proximity labeling with enhanced direct identification of biotinylation sites. *Commun. Biol.* **7**, 554 (2024).
19. Singh, R. et al. Proteomic insights into early-stage Alzheimer's disease: Identifying key neuronal proteins impacted by amyloid beta oligomers in an in vitro model. *Neuroscience* **560**, 254–262 (2024).
20. Gage, F. H. et al. Survival and differentiation of adult neuronal progenitor cells transplanted to the adult brain. *Proc. Natl. Acad. Sci. USA* **92**, 11879–11883 (1995).
21. Meng, H. et al. Quiescent adult neural stem cells: developmental origin and regulatory mechanisms. *Neurosci. Bull.* **40**, 1353–1363 (2024).
22. Lipovsek, M. & Grubb, M. S. Boosting adult neurogenesis to enhance sensory performance. *EMBO J.* **38**. <https://doi.org/10.15252/embj.2019101589> (2019).
23. Tamai, S., Sanada, K. & Fukada, Y. Time-of-day-dependent enhancement of adult neurogenesis in the hippocampus. *PLoS ONE* **3**, e3835 (2008).
24. Cribbs, A. P., Kennedy, A., Gregory, B. & Brennan, F. M. Simplified production and concentration of lentiviral vectors to achieve high transduction in primary human T cells. *BMC Biotechnol.* **13**, 98 (2013).
25. Su, Y. et al. Study of FOXO1-interacting proteins using TurboID-based proximity labeling technology. *BMC Genom.* **24**, 146 (2023).
26. Baltusaitis, E. E. et al. Interaction between the mitochondrial adaptor MIRO and the motor adaptor TRAK. *J. Biol. Chem.* **299**, 105441 (2023).
27. Lopez-Domenech, G. et al. Miro proteins coordinate microtubule- and actin-dependent mitochondrial transport and distribution. *EMBO J.* **37**, 321–336 (2018).
28. Misko, A., Jiang, S., Wegorzewska, I., Milbrandt, J. & Baloh, R. H. Mitofusin 2 is necessary for transport of axonal mitochondria and interacts with the Miro/Milton complex. *J. Neurosci.* **30**, 4232–4240 (2010).
29. Niescier, R. F., Hong, K., Park, D. & Min, K. T. MCU Interacts with Miro1 to modulate mitochondrial functions in neurons. *J. Neurosci.* **38**, 4666–4677 (2018).
30. Fransson, S., Ruusala, A. & Aspenstrom, P. The atypical Rho GTPases Miro-1 and Miro-2 have essential roles in mitochondrial trafficking. *Biochem. Biophys. Res. Commun.* **344**, 500–510 (2006).
31. Perinan, M. T. et al. The role of RHOT1 and RHOT2 genetic variation on Parkinson disease risk and onset. *Neurobiol. Aging* **97**, 144 e141–144 e143 (2021).
32. Ren, X. et al. MIRO-1 interacts with VDAC-1 to regulate mitochondrial membrane potential in *Caenorhabditis elegans*. *EMBO Rep.* **24**, e56297 (2023).
33. Wiley, S. E., Murphy, A. N., Ross, S. A., van der Geer, P. & Dixon, J. E. MitoNEET is an iron-containing outer mitochondrial membrane protein that regulates oxidative capacity. *Proc. Natl. Acad. Sci. USA* **104**, 5318–5323 (2007).
34. Lin, J., Zhou, T., Ye, K. & Wang, J. Crystal structure of human mitoNEET reveals distinct groups of iron sulfur proteins. *Proc. Natl. Acad. Sci. USA* **104**, 14640–14645 (2007).
35. Kwak, C. et al. Contact-ID, a tool for profiling organelle contact sites, reveals regulatory proteins of mitochondrial-associated membrane formation. *Proc. Natl. Acad. Sci. USA* **117**, 12109–12120 (2020).
36. Ham, S. J. et al. PINK1 and Parkin regulate IP(3)R-mediated ER calcium release. *Nat. Commun.* **14**, 5202 (2023).
37. Jiang, Y., Yu, Y., Pan, Z., Glandorff, C. & Sun, M. Ferroptosis: a new hunter of hepatocellular carcinoma. *Cell Death Discov.* **10**, 136 (2024).
38. Geldenhuys, W. J. et al. Loss of the mitochondrial protein mitoNEET in mice is associated with cognitive impairments and increased neuroinflammation. *J. Alzheimers Dis.* **103**, 429–440 (2025).
39. Martinez, A. et al. Mitochondrial CISD1/Cisd accumulation blocks mitophagy and genetic or pharmacological inhibition rescues neurodegenerative phenotypes in Pink1/parkin models. *Mol. Neurodegener.* **19**, 12 (2024).
40. Iwata, R. et al. Mitochondrial dynamics in postmitotic cells regulate neurogenesis. *Science* **369**, 858–862 (2020).
41. Soares, R. et al. Lineage-specific changes in mitochondrial properties during neural stem cell differentiation. *Life Sci. Alliance* **7**, e202302473 (2024).
42. Ha, S. et al. Autophagy mediates astrogenesis in adult hippocampal neural stem cells. *Exp. Neurobiol.* **28**, 229–246 (2019).
43. Cho, K. F. et al. Split-TurboID enables contact-dependent proximity labeling in cells. *Proc. Natl. Acad. Sci. USA* **117**, 12143–12154 (2020).

## Acknowledgements

This work was supported by grants from the Basic Science Research Program through the National Research Foundation of Korea [RS-2025-00563415 to H. Lee], [2021R111A1A01048638 to HN. Woo] and [2022R1A2C1009376 to JY. Mun] and supported by the National Science Challenge Initiatives [RS-2024-00419699 to JY. Mun] through National Research Foundation (NRF) grants funded by the Ministry of Science and ICT (MSIT), Korea.

## Author contributions

H.L., J.Y.M., and H.N.W. supervised the study; I.K.K., T.K.M., A.R.H., and C.K. performed the in vitro experiments and analyzed the data; I.K.K., H.N.W., M.K.J., J.K.S., and H.W.R. designed the experiments, and I.K.K., H.N.W., S.L., and C.K. wrote the paper. H.L., J.Y.M., A.R.H., D.B.Y., and S.W.K. reviewed and edited the manuscript. All the authors have read and agreed to the published version of the manuscript.

## Competing interests

The authors declare no competing interests.

## Additional information

**Supplementary information** The online version contains supplementary material available at <https://doi.org/10.1038/s42003-025-08990-0>.

**Correspondence** and requests for materials should be addressed to Ha-Na Woo, Ji Young Mun or Heuiran Lee.

**Peer review information** *Communications Biology* thanks Ruben Dagda and the other, anonymous, reviewer(s) for their contribution to the peer review of this work. Primary Handling Editors: Ibrahim Javed and Joao Valente. A peer review file is available.

**Reprints and permissions information** is available at <http://www.nature.com/reprints>

**Publisher's note** Springer Nature remains neutral with regard to jurisdictional claims in published maps and institutional affiliations.

**Open Access** This article is licensed under a Creative Commons Attribution-NonCommercial-NoDerivatives 4.0 International License, which permits any non-commercial use, sharing, distribution and reproduction in any medium or format, as long as you give appropriate credit to the original author(s) and the source, provide a link to the Creative Commons licence, and indicate if you modified the licensed material. You do not have permission under this licence to share adapted material derived from this article or parts of it. The images or other third party material in this article are included in the article's Creative Commons licence, unless indicated otherwise in a credit line to the material. If material is not included in the article's Creative Commons licence and your intended use is not permitted by statutory regulation or exceeds the permitted use, you will need to obtain permission directly from the copyright holder. To view a copy of this licence, visit <http://creativecommons.org/licenses/by-nc-nd/4.0/>.

© The Author(s) 2025